Middle Eocene Climatic Optimum (MECO) and its imprint in the continental Escanilla Formation, Spain

Nikhil Sharma[1,2], Jorge E. Spangenberg[3], Thierry Adatte[4], Torsten Vennemann[3], László Kocsis[3], Jean Vérité[1,5], Luis Valero[1,6], Sébastien Castelltort[1]

[1]Department of Earth Sciences, University of Geneva, Rue des Maraichers 13, 1205 Geneva, Switzerland

[2]Bureau of Economic Geology, The University of Texas at Austin, Austin, TX 78712 USA

[3]Institute of Earth Surface Dynamics (IDYST), University of Lausanne, Géopolis, 1015 Lausanne, Switzerland

[4]Institute of Earth Sciences (ISTE), University of Lausanne, Géopolis, 1015 Lausanne, Switzerland

[5]LPG – Le Mans, UFR Sciences et Techniques, Université du Maine, 72089 Le Mans cedex 9, France

[6]Departament de Dinàmica de la Terra i l'Oceà, Facultat de Ciències de la Terra, Barcelona, 08028, Spain

Correspondence to: Nikhil Sharma (nikhil.sharma@beg.utexas.edu)

Abstract. The Middle Eocene Climatic Optimum (MECO) is a global warming event mainly recognized in the marine domain but described less from the terrestrial environment. Here we present a comprehensive geochemical record of the MECO from the Escanilla Formation, a fluvial sedimentary succession in the southern Pyrenees, Spain, based on a suite of sampled paleosols, fluvial stromatolites and pedogenic nodules. Our multiproxy approach involves using carbon and oxygen stable isotope compositions to identify the regional preservation of the MECO, calculate chemical weathering intensity and mean annual precipitation, perform clumped isotopes on carbonates and identify clay mineralogy assemblages of paleosols. Results indicate that the Middle Eocene interval in the southern Pyrenees was characterized by low weathering rates under warm and arid climatic conditions. This is further supported by the presence of smectite, palygorskite, illite, and chlorite, which suggest seasonal rainfall but under generally dry conditions resulting in weak chemical weathering. Importantly, a negative organic carbon isotopic excursion indicates the regional, terrestrial impact of the MECO, highlighting that fluvial sedimentary successions even in active foreland basins can represent particularly interesting terrestrial archives of past changes in global climate.

1 Introduction

The Middle Eocene Climatic Optimum (MECO) is a transient global warming event that occurred during the Bartonian (40.0 Ma) and represents a significant reversal in the long-term cooling trend of the Middle to Upper Eocene (Bohaty et al., 2009). It is characterized by a distinct negative oxygen isotope excursion (OIE) of about 1 ‰ interpreted as a 3 to 6 °C rise in global ocean temperatures, and a subdued and spatially non-uniform negative carbon isotope excursion (CIE) in marine carbonates (e.g., Bohaty et al., 2009; Bijl et al., 2010; Henehan et al., 2020). This lack of a distinct negative and robust CIE, a key diagnostic feature of earlier Cenozoic hyperthermals such as the Paleocene Eocene Thermal Maximum (PETM), its comparatively long duration (~500 Kyr), along with elevated pCO_2 levels sustained over a long period by a diminished silicate weathering feedback (van der Ploeg et al., 2018), points towards an instability in the long-term carbon cycle during the MECO (Sluijs et al., 2013). In principle, elevated global temperatures and CO_2 levels are expected to be reflected in continental environments in the form of increased silicate weathering of exposed rocks. This process helps restore the climate through a drawdown of atmospheric CO_2 typically associated with an intensified hydrological cycle (e.g., Sluijs et al., 2013; Methner et al., 2016; van der Ploeg et al., 2018).

While the MECO has been extensively identified in both onshore and offshore marine sedimentary sections (e.g., Jovane et al., 2007; Bohaty et al., 2009; Spofforth et al., 2010; Gandolfi et al., 2023), only a few studies have identified it in terrestrial successions (e.g., Bosboom et al., 2014; Mulch et al., 2015; Methner et al., 2016). Currently available data from the terrestrial realm suggests important regional differences in response to the MECO. For instance, Bosboom et al. (2014) discuss the onset of region-wide arid conditions in the Xining Basin, China, while Methner et al. (2016) predicted large temperature seasonality and an intensification of the hydrologic cycle in the continental interiors of north-western America. These regional differences highlight the need to further document records of the MECO in continental depositional systems to provide more constraints for understanding the dynamics of the climate and Earth's surface perturbations during that period.

To contribute to this issue, we document a new record in the Escanilla Formation (Fm), a fluvial sedimentary succession in the southern Pyrenees at Olsón (Spain), using carbon stable isotope compositions ($\delta^{13}C$) of paleosol organic matter to highlight the regional preservation of the MECO. We also measured the carbon and oxygen stable isotope ratios of carbonates in stromatolites, pedogenic nodules, and bulk paleosols to further examine the terrestrial MECO-related changes in the carbon and water cycles. We calculated weathering indices to quantify weathering intensity during the MECO, and reconstructed climatic conditions using mean annual precipitation estimates, preliminary carbonate clumped isotope thermometry data, and clay mineralogy.

2 Study locality and age constraints

2.1 The Escanilla sediment routing system

60 The Escanilla sediment routing system, situated in the Pyrenees, represents a well-preserved mid- to late Eocene-age (ca. 41 – 34 Ma) fluviatile succession. Catchment areas of the high Pyrenees were linked to the southern Pyrenean foreland Basin through the Sis and Gurb paleovalleys (Figure 1A) (Bentham et al., 1993; Labourdette & Jones 2007; Labourdette 2011; Michael et al., 2013). Extensive paleocurrent data suggests that these paleovalley systems predominantly derived sediments from the axial zone of the Pyrenees, converging in the

65 Viacamp area (Figure 1A). From this point, sediments were carried downstream to the west through the Ainsa Basin (Vincent 2001; Whittaker et al., 2011; Parsons et al., 2012; Michael et al., 2013) into the shallow marine Jaca Basin (Peris Cabré et al., 2023) (Figure 1A).

The entire Escanilla sediment routing system has been meticulously documented within a comprehensive source-to-sink framework based on provenance tools, including clast lithologies (Mesozoic carbonates, Upper

70 Carboniferous to Triassic clastic and igneous rocks, Hercynian granites, Paleozoic basement), heavy minerals, U–Pb geochronology of detrital zircons, apatite fission track analysis, paleocurrent analysis, magneto and biostratigraphy. Detailed explanation of this system can be found in the works of Michael et al. (2013, 2014) and references therein.

2.2 Escanilla Fm

75 The Escanilla Fm at Olsón has a maximum thickness of 1000 m and is subdivided into the Mondot and Olsón members (Figure 1C) (e.g., Labourdette & Jones, 2007). At the transition of these two members lies a basin-wide extending conglomeratic channel-complex, hereafter referred to as the Olsón Conglomerate (OC), which is the interpreted stratigraphic expression of peak MECO warming in the Escanilla Fm based on available age constraints (Figures 1B–1E). The Escanilla Fm predominantly consists of conglomeratic to sandy channel-fill

80 deposits and their adjacent fine-grained floodplain/overbank deposits. These floodplain fines have been previously characterized as Entisols, displaying a low degree of pedogenesis (Dreyer et al., 1992). On the field, paleosols were identified based on pedogenic features such as horizonation, coloring, root traces, and burrowing. In addition, we document the presence of three pedogenic carbonate nodule horizons (Figure 2C) and nine fluvial stromatolites preserved within the Escanilla floodplains (Figures 2D–2F). Although fluvial stromatolites are common in the

85 upper Paleocene to Eocene fluvial deposits of Spain (Zamarreno et al., 1997), to our knowledge, they have not been identified in the Escanilla Fm before. These stromatolites have been preserved as elongated domes with an asymmetrical shape and have varying lengths from a few centimeters to a meter, and in diameter from 15 to 60 cm. They have been interpreted as having formed as overbank deposits of fluvial channels with a preferential

elongation presumably parallel to the flow direction (Zamarreno et al., 1997). These stromatolites are also similar in appearance to Eocene stromatolites that grew on tree trunks from the Green River Formation, Colorado, USA (Awramik et al., 2015), although further research would be required to investigate this.

Within this context, a composite section of about 120 m was sampled for a suite of paleosol (ca. 200 g of fine-grained and fresh (unweathered) rock) and carbonate (pedogenic nodules and stromatolites) samples, collected below the weathering depth (at least 20 cm below modern surface) to avoid samples that could have been affected by diagenesis and may have altered grain size distribution (e.g., Lupker et al., 2011). Locations of sampled sites and corresponding raw data from different analyses have been provided as supplementary material.

2.3 Age constraints

The age model used in this study is based on the magnetostratigraphic framework, involving high- and intermediate-quality samples, of the Escanilla Fm by Vinyoles et al., (2020) and agrees well with the magnetostratigraphic interpretation of Bentham et al., (1992). Age constraints by Vinyoles et al., (2020) were also recently used by Peris Cabré et al., (2023) for the identification of the MECO at Belsue and Yebra de Basa in the Jaca Basin.

To compare our geochemical data relative to the target MECO isotopic excursion from ODP site 738 (Bohaty et al. (2009)) and the Geomagnetic Polarity Time Scale (GPTS 2020) (Ogg 2020), we rely on a preliminary first-order linear scaling by matching the base (at 40 m) and top (at 210 m) of Chron C18n in the magnetostratigraphic data of Vinyoles et al., (2020), to the base of Chron C18n.2n and top of Chron C18n.1n on the Geomagnetic Polarity Time Scale (GPTS 2020) (Figure 1E). All data are presented relative to the thickness of the sampled Olsón section accompanied by the local magnetostratigraphic interpretation of Vinyoles et al., (2020), linearly scaled to the GPTS 2020.
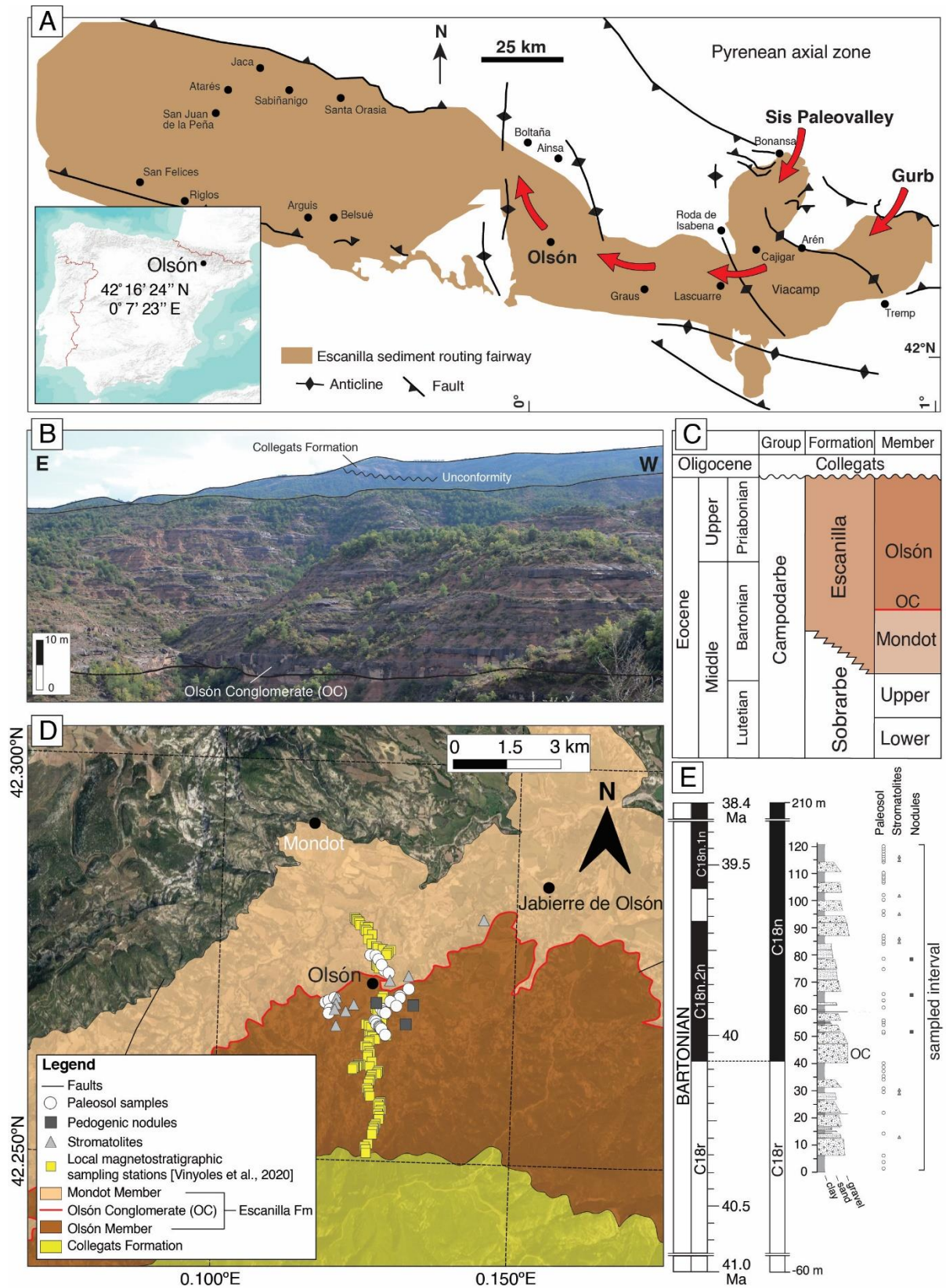
110

Figure 1 **(A)** Map of the Escanilla paleo-sediment routing system in the southern Pyrenees, Spain, also showing the main

tectonic structures. Red arrows mark the water discharge and sediment transport direction of the Escanilla system away from

the source regions of Sis and Gurb paleovalleys in the axial zone of the Pyrenees. Figure modified after Michael et al. (2014a).

Also displayed is an inset map of Spain, indicating the study area near the village of Olsón. Map modified from Labourdette

115 & Jones (2007). **(B)** Field image depicting the sampled Escanilla Fm. **(C)** Lithostratigraphic framework of the Escanilla Fm

at Olsón consists of two main Members – the Mondot and the Olsón members with the Olsón Conglomerate (OC, red line) at

the transition between the two Members. **(D)** Geological map of the Escanilla Formation around Olsón. This map was prepared

using QGIS Desktop 3.22.8 (https:// qgis. org/ en/ site/). **(E)** Sampled composite section, with position of each collected

sample, of the Escanilla Fm together with the local magnetostratigraphic interpretation by Vinyoles et al. (2020) correlated to

120 the Geomagnetic Polarity Time Scale (GPTS 2020) (Ogg, 2020). The thickest normal magnetozone C18n in the local

magnetostratigraphic interpretation includes C18n.1n, C18n.1r, and C18n.2n.
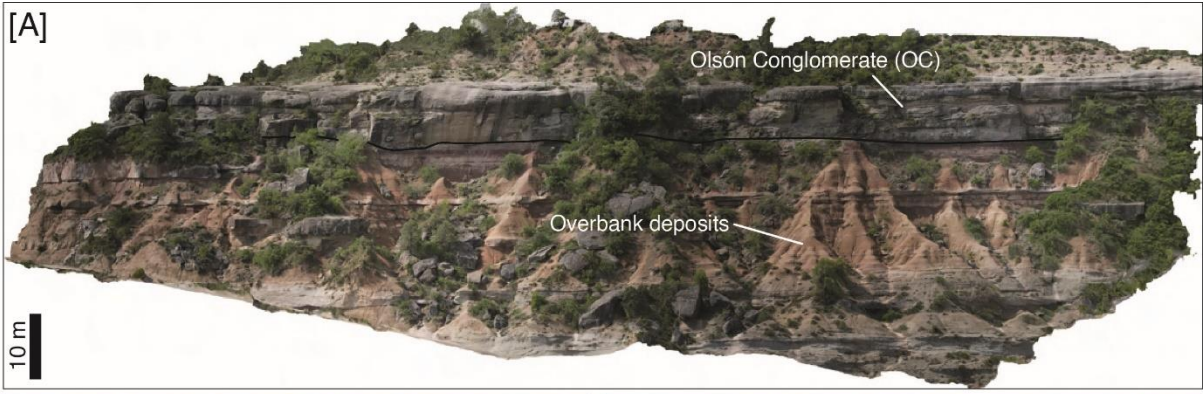
Figure 2. **(A)** Outcrop panorama depicting the Olsón Conglomerate (OC) and the thick floodplain interval sampled for paleosols. **(B)** A typical sampled paleosol. **(C)** Pedogenic carbonate nodules sampled below the weathering depth. **(D)** Long, tubular fluvial stromatolites (indicated by arrows) preserved in the floodplain. **(E, F)** Cross-section of stromatolite samples NS7 and NS1 respectively, showing the well preserved individual layering. The white stars indicate micro-drilling sites.

3 Material and methods

Analyses were carried out on a suite of sampled paleosols (N = 45), stromatolites (n = 9), and pedogenic nodules (n = 9 from 3 sample horizons) (Figure 1D). Pedogenic nodules were small and could not be cut open to be examined by cathodoluminescent microscopy or transmitted light. Hence, entire nodules were crushed, and their homogenized powders were used for analysis.

Powders of bulk paleosol samples were prepared and analyzed for geochemical indicators, including total organic carbon (TOC) content, Rock-Eval parameters, organic carbon isotope compositions ($\delta^{13}C_{org}$), carbonate carbon and oxygen isotopes ($\delta^{13}C_{carb}$ and $\delta^{18}O_{carb}$), major elements, and clay mineral assemblages. Stromatolite and pedogenic nodule powders were analyzed for $\delta^{13}C_{carb}$ and $\delta^{18}O_{carb}$ and clumped isotope compositions (δ^{47} and Δ_{47}).

3.1 Rock eval analysis

Rock eval pyrolysis was performed at the Institute of Earth Sciences of the University of Lausanne (ISTE-UNIL) to assess the total organic carbon (TOC) content in the paleosols. The analyses were performed using a Rock-Eval 6 instrument, following the procedure described by Behar et al. (2001).

3.2 Organic carbon isotopes

The carbon isotope compositions of organic matter in paleosol samples were analysed in the stable isotope laboratories of the Institute of Earth Surface Dynamics, University of Lausanne (IDYST-UNIL). Samples first underwent de-carbonatation with 10 % v/v HCl, then thoroughly washed with deionized water and dried at 40 °C for 48 h. The $\delta^{13}C_{org}$ measurements were made using a Carlo Erba 1100 (Fisons Instruments, Milan, Italy) elemental analyser connected to a Thermo Fisher Scientific Delta V Plus isotope ratio mass spectrometer, both operated under continuous helium flow. Measured $\delta^{13}C$ values were calibrated and normalized using international reference materials and in-house standards (Spangenberg 2006, 2016) and reported in per mil (‰) vs. Vienna Pee Dee Belemnite limestone standard (VPDB). The precision of the $\delta^{13}C_{org}$ values were better than 0.1 ‰.

3.3 Carbonate isotopes

Carbon and oxygen isotope compositions were determined at the IDYST-UNIL laboratories. Bulk paleosol samples containing >10 Wt.% $CaCO_3$, including carbonate samples, were analysed using a Thermo Fisher Scientific Gas Bench II carbonate preparation device connected to a Delta V Plus isotope ratio mass spectrometer according to a method adapted after Spötl & Vennemann (2003). CO_2 gas was produced by reaction with 99 % orthophosphoric acid at 70 °C. The $\delta^{13}C_{carb}$ and $\delta^{18}O_{carb}$ values are reported in ‰ vs. VPDB. Replicate measurements of the international calcite standard NBS 19 (limestone, $\delta^{13}C$ = +1.95 ‰, $\delta^{18}O$ = –2.19 ‰) and an in-house standard (Carrara marble, $\delta^{13}C$ = +2.05 ‰, $\delta^{18}O$ = –1.7 ‰) yielded an analytical precision (1 σ) of ± 0.05 ‰ for $\delta^{13}C_{carb}$ and ± 0.1 ‰ for $\delta^{18}O_{carb}$.

3.4 Major elements

SiO_2, Al_2O_3, Fe_2O_3, MnO, MgO, CaO, Na_2O, K_2O, P_2O_5, Cr_2O_3, NiO, and loss on ignition (LOI), were measured in the powdered bulk paleosol samples by X-ray fluorescence (XRF; Phillips PANalytical PW2400 spectrometer) at the ISTE-UNIL laboratories. The analyses were performed on fused glass discs prepared with 1.2000 ± 0.0005 g ignited sample powder and 6.0000 ± 0.0005 g of lithium tetraborate ($Li_2B_4O_7$). The concentrations of the major elements were expressed as Wt. % oxides. The analytical precision (1 σ) assessed by replicate analyzed of international reference materials is 0.4 %.

3.5 Weathering indices

The chemical index of alteration (CIA in %; Eq. 1), proposed by Nesbitt & Young (1982), was used to quantify the degree of weathering by using the molar ratio of immobile Al_2O_3 and the mobile oxides CaO, Na_2O, and K_2O in the silicate fraction (e.g., Deng et al., 2022). The CIA is commonly used to estimate the intensity of alteration and test for environmental factors (e.g., temperature, precipitation, elevation, slope) affecting silicate weathering.

$$CIA = \frac{Al_2O_3}{Al_2O_3 + Na_2O + CaO^* + K_2O} \times 100 \qquad (1)$$

, where CaO* is the CaO incorporated in the silicate fraction and is calculated as:

$$CaO^* = CaO - [(10/3) \times P_2O_5] \qquad (2)$$

Intense weathering removes mobile oxides, concentrating Al_2O_3 to a maximum value of almost 100 Wt.%; whereas weak weathering would give lower CIA values (<50 %) because of dominance of mobile oxides.

For comparison to the CIA, we used the chemical index of weathering (CIW in %; Eq. 3) proposed by Harnois, (1988), which is a modified version of the CIA to account for potassium metasomatism in paleosols during weathering (Stein et al., 2021) (See supplementary material, Figure S7).

$$CIW = \frac{Al_2O_3}{Al_2O_3 + Na_2O + CaO^*} \times 100 \tag{3}$$

185   , where CaO* is the CaO incorporated in the silicate fraction (Eq. 2).

3.6 Mean annual precipitation

Mean annual precipitation (MAP) was estimated from the CIW (Eq. 4; standard error $= \pm$ 182 mm yr^{-1}) using the equation proposed by Sheldon et al. (2002) as:

190

$$MAP = 221e^{0.0197(CIW)} \tag{4}$$

3.7 Clumped (Δ_{47}) isotopes

Clumped isotope compositions were measured at the IDYST-UNIL laboratories, using a Nu Perspective dual-inlet mass spectrometer with an automated NuCarb sample preparation device. Carbonate digestion, CO_2

195   purification procedure, and measurements followed Anderson et al. (2021). For Δ_{47} analyses, 3.8 to 4.2 mg of carbonate were reacted at 70 °C with 110 µl 105 Wt.% phosphoric acid (H_3PO_4), and the liberated CO_2 was purified after digestion in a series of temperature-controlled, liquid-nitrogen-cooled cold fingers, including an adsorption trap (packed with Porapak Q 50/80 mesh) held at -30 °C. We applied the acid fractionation factor of +0.088 ‰ (Anderson et al., 2021) to the data in order to compare with the ETH-standards reacted at 90 °C

200   (Bernasconi et al., 2021).

Three standards (ETH-1, ETH-2, ETH-3) have been used to calculate Δ_{47} values of unknown samples using linear regression with the respective Δ_{47} values of 0.205, 0.209, and 0.613 (Bernasconi et al., 2021). Temperatures are calculated using the calibration of Anderson et al. (2021), where Δ_{47} is in ‰ and T in °C, as:

$$\Delta_{47} = (0.0391 \pm 0.0004) \times (10^6/T^2) + (0.154 \pm 0.004)$$

205   Multiple analyses were carried out on the drilled powders of eachstromatolites (n = 2 to 4) and pedogenic nodules (n= 4 to 8) samples, to obtain better statistics (data in supplementary material).

3.8 Clay mineralogy

Clay mineralogical assemblages in paleosol samples were determined by X-ray diffractometry (XRD) at the ISTE-

210   UNIL laboratories. Samples were prepared following the procedure described in Adatte et al. (1996). Analyses

were made using a Thermo Fisher Scientific ARL X-TRA diffractometer and the intensities of the XRD peaks characteristic of each mineral, were used to estimate the relative percentage in bulk rock and < 2 µm and 2–16 µm clay size fractions.

215 **3.9 Uncertainty on reported data**

All data reported in this study is associated with uncertainties in the form of standard error of the mean (SE) calculated as $SE = \frac{SD}{\sqrt{n}}$, where SD is the standard deviation and n is the number of replicates analyzed. Uncertainty propagation was done using the uncertainites package on Python (Spyder 4.0.1), which is an open-source and cross-platform program that handles calculations with numbers involving uncertainties.

220

4 Results and discussion

4.1 TOC content and δ^{13}C of bulk paleosol organic matter

TOC content in paleosol samples varies from 0.01 ± 0.01 to 0.57 ± 0.01 Wt. % with an average value of 0.07 ± 0.01 Wt. % (N = 45) (Figure 3). Low TOC may be indicative of low primary productivity, in this case 'vegetation'

225 including grasses and higher plants, and (cyno)bacteria or low preservation of organic matter due to an oxidizing (oxygenated) environment (Tyson, 1995).

The $\delta^{13}C_{org}$ values of the paleosols have a range between -26.0 ± 0.2 and -20.4 ± 0.2 ‰ with an average value of -23.2 ± 0.2 ‰ (N = 45) (Figure 3). A negative CIE is marked by a 3 ‰ shift from the base of the section (from 0 to 30 m), where the onset begins, followed by a plateau of low values (30 to 50 m) that gradually return to higher

230 values 60 m upwards. This negative CIE is most likely coeval to the 0.5 ‰ negative excursion observed in the benthic foraminifera $\delta^{13}C_{cib}$ values from ODP sites 738 (Bohaty et al., 2009) (Figure 3), indicating a general agreement in the change of δ^{13}C values, even though absolute differences in the magnitude of excursions exist.

A similar large magnitude negative CIE was previously identified for the PETM within the intermontane Piceance Creek Basin of western Colorado (USA), where a negative CIE of about 3 ‰ was reported (Foreman et al., 2012).

235 The $\delta^{13}C_{org}$ record from the Middle Eocene Alano di Piave section deposited in the marginal Tethys Ocean recorded a negative CIE of about 1 ‰ (Spofforth et al., 2010) while the coeval shallow water Sealza section from Italy recorded a negative CIE of 2 ‰ (Gandolfi et al., 2023).
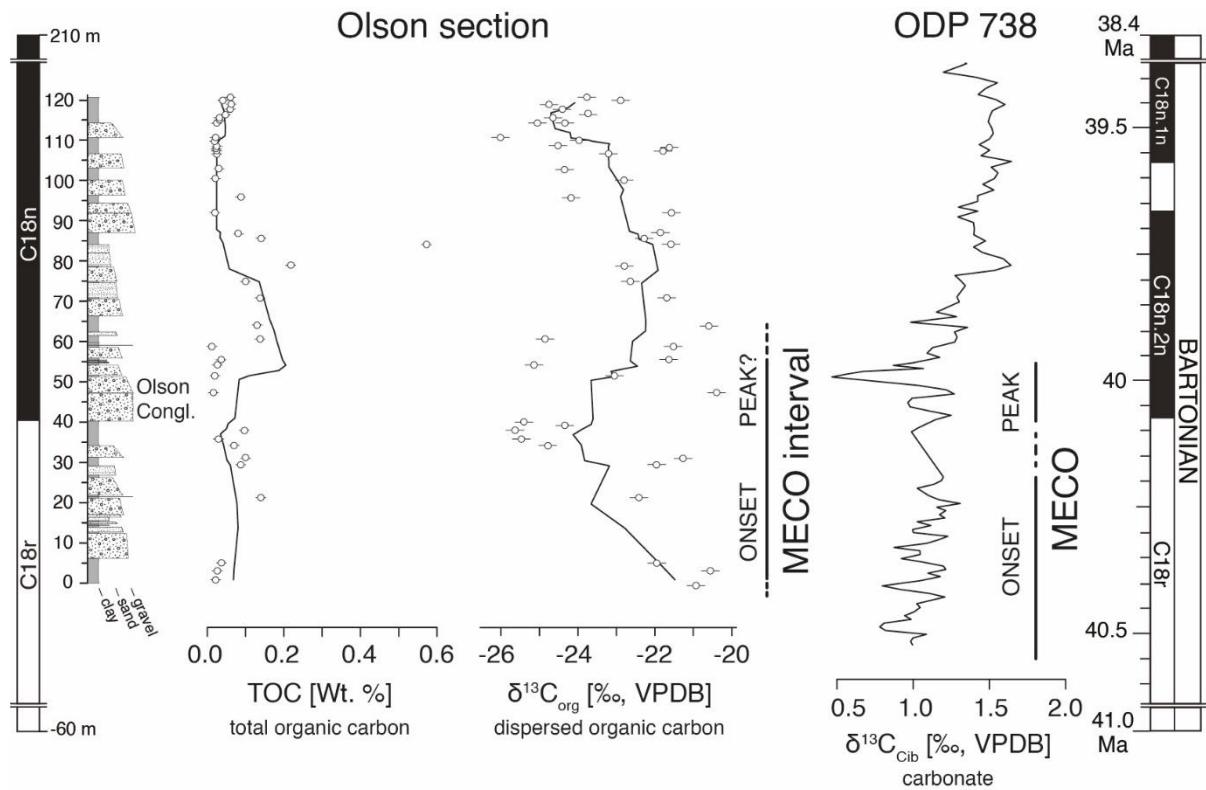
Figure 3. Total organic carbon (TOC) and dispersed organic carbon isotope compositions ($\delta^{13}C_{org}$), and associated standard error, in paleosol samples (white circles) presented with a 7-point moving average. Also displayed is the change in benthic foraminiferal (genus *Cibicidoides*) carbon isotope ratios ($\delta^{13}C_{Cib}$) from ODP site 738.

The $\delta^{13}C_{org}$ values can also be used as indicators of paleoecology and paleoclimate (Kohn, 2010). C$_3$ plants which include trees, most shrubs and cool season grasses, have $\delta^{13}C$ values between -37 ‰ and -20 ‰ and have dominated the history of terrestrial vegetation (Kohn, 2010). This wide range in $\delta^{13}C$ values of plants is dependent on several factors such as temperature, altitude, latitude, and MAP (Schulze et al., 1996; Kohn, 2010). Non water-stressed C$_3$ plants are enriched in ^{12}C and hence have more negative $\delta^{13}C$ values, typically lower than -26 ‰. Higher $\delta^{13}C$ values (> -26 ‰) are associated with plants growing under water deficient conditions and low soil transpiration rates (MAP < 500 mm yr^{-1}) (e.g., Cerling & Quade 1993; Kohn, 2010; Methner et al., 2016). Measured $\delta^{13}C_{org}$ values suggest a predominance of C$_3$ vegetation, consistent with an Eocene ecosystem (Cerling & Quade 1993; Methner et al., 2016). A significant proportion of measured values have relatively high $\delta^{13}C$ values (> -23 ‰) that are characteristic of dry environments with MAP < 500 mm yr^{-1} (Kohn, 2010). Low primary productivity and low organic matter preservation complemented by elevated $\delta^{13}C_{org}$ values likely indicates sparse vegetation in a dry and arid ecosystem.

255 Vegetation plays a key role in influencing landscape response to terrestrial hydroclimates during global warming events such as the PETM (Foreman et al., 2012). For instance, de-vegetated fluvial banks enhance sediment erodibility, bank erosion, and lateral channel mobility, resulting in peak discharge and bedload sediment downstream flux even under a negligible increase in precipitation (Gran et al., 2001; Barefoot et al., 2021). Sparse vegetation in the fluvial Escanilla Fm reflects the response of the Escanilla rivers to peak discharge and sediment

260 flux events, which modified the stratigraphic architecture described as alternating sequences of high amalgamation (HA) and low amalgamation (LA) intervals (Sharma et al., 2023). Such large flux in the Escanilla Fm at Olsón during the MECO is also consistent with the clastic progradation event observed in the Jaca Basin (Peris Cabré et al., 2023), indicating the transmission and preservation of sedimentary flux signals in the sedimentary record from source-to-sink. Lastly, enhanced channel mobility during the MECO could also have lead to the export of large

265 quantities of fine-grained (floodplain) sediment to the marine domain and potentially affected the carbonate environments developing at that time on the southern Margin of the Jaca-Pamplona trough (e.g. Garcès et al., 2023).

4.2 δ^{13}C and δ^{18}O of paleosol bulk carbonates, stromatolites and pedogenic nodules

270 The δ^{13}C$_{carb}$ values in paleosol bulk carbonates have a range of -2.6 ± 0.01 to -1.0 ± 0.01 ‰ with an average of - 1.6 ± 0.01 ‰ (N = 45) (Figure 4). A transient decrease in δ^{13}C$_{carb}$ values is observed at 40 m where a negative CIE of about 1.0 ‰ magnitude is considered to represent the MECO negative CIE in the Escanilla Fm, followed by an increase in δ^{13}C$_{carb}$ values to -1.5 ‰ towards the top of the section (Figure 4). These values are most likely synchronous to the negative CIE recorded in paleosol organic matter.

275 δ^{13}C$_{carb}$ values in stromatolites range from -3.9 ± 0.1 to -1.3 ± 0.1 ‰ with an average value of -2.5 ± 0.1 ‰ (N = 63, 5 to 9 replicate measurements from 9 sample horizons), while δ^{13}C$_{carb}$ values in pedogenic nodules range from -4.9 ± 0.3 ‰ to -1.1 ± 0.3 ‰ with an average value of -3.2 ± 0.3 ‰ (N = 29, 9 to 10 replicate measurements from 3 sample horizons). Since sample size is limited stratigraphically, it does not permit a direct evaluation of the isotopic signal relative to the MECO. However, δ^{13}C$_{carb}$ values from stromatolites and pedogenic nodules show a

280 consistent 1 to 2 ‰ negative offset when compared to values from paleosol bulk carbonates, which is possibly due to the presence of detrital Mesozoic carbonates (δ^{13}C$_{carb}$ = 0 ‰; Zamarreno et al., 1997) in the bulk sediments from the source area.
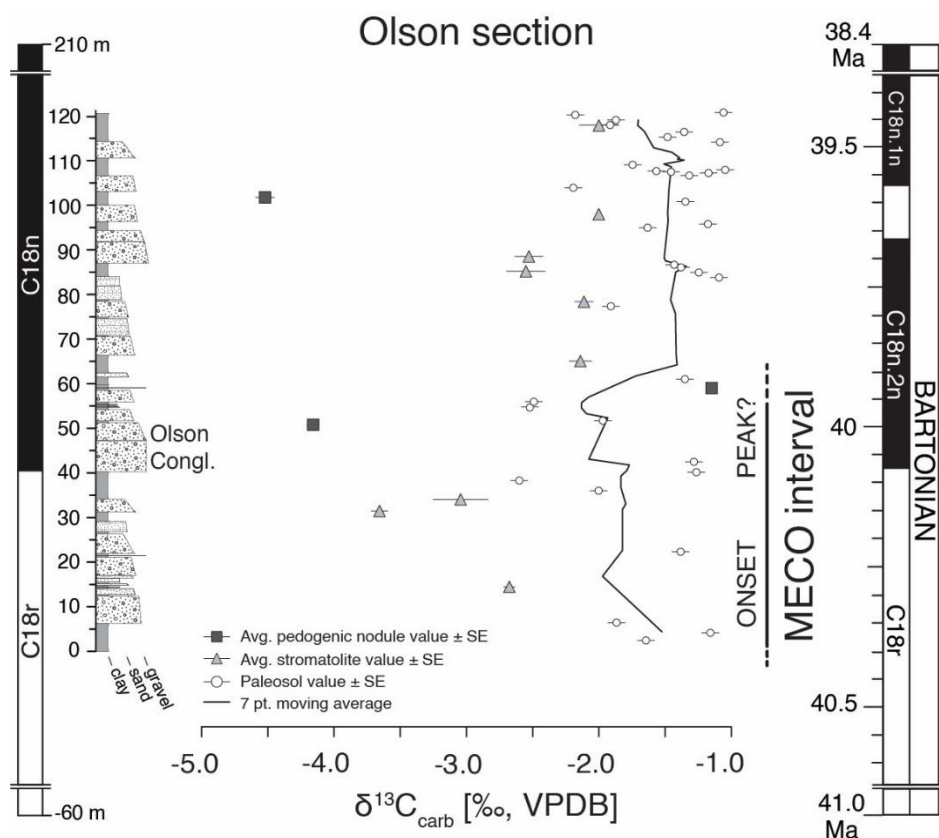
Figure 4. Carbon isotope compositions ($\delta^{13}C_{carb}$) and associated standard error from paleosol bulk carbonates (white circles) with a 7-point moving average, and from stromatolite (triangles) and pedogenic nodules (squares) for the Olsón section. Also marked is the MECO onset and peak interval based on $\delta^{13}C_{org}$ values from this study.

The $\delta^{18}O_{carb}$ values in paleosol bulk carbonates have a range between -6.7 ± 0.1 and -4.2 ± 0.1 ‰ with an average of -5.8 ± 0.1 ‰ (N = 45) (Figure 5). A positive OIE of ca 0.5 ‰ magnitude at 40 to 60 m, suggests an increase in freshwater ^{18}O content and perhaps represents peak MECO conditions in the Escanilla Fm. Peak warming would correspond to the OC where highest discharge and flux estimates have been predicted by Sharma et al. (2023). Following the positive OIE, $\delta^{18}O_{carb}$ values decline and return to relatively stable values of around -6.0 ‰, 60 m onwards until the top of the Olsón section and may represent the post-MECO cooling phase (Figure 5).

$\delta^{18}O_{carb}$ values in stromatolites range from -8.1 ± 0.1 to -4.7 ± 0.1 ‰ with an average value of -7.1 ± 0.1 ‰ (N = 63), while $\delta^{18}O_{carb}$ values in pedogenic nodules range from -7.6 ± 0.1 ‰ to -6.5 ± 0.1 ‰ with an average value of -6.9 ± 0.1 ‰ (N = 29); and crudely match the $\delta^{18}O$-trend in paleosol bulk carbonates (Figure 5).
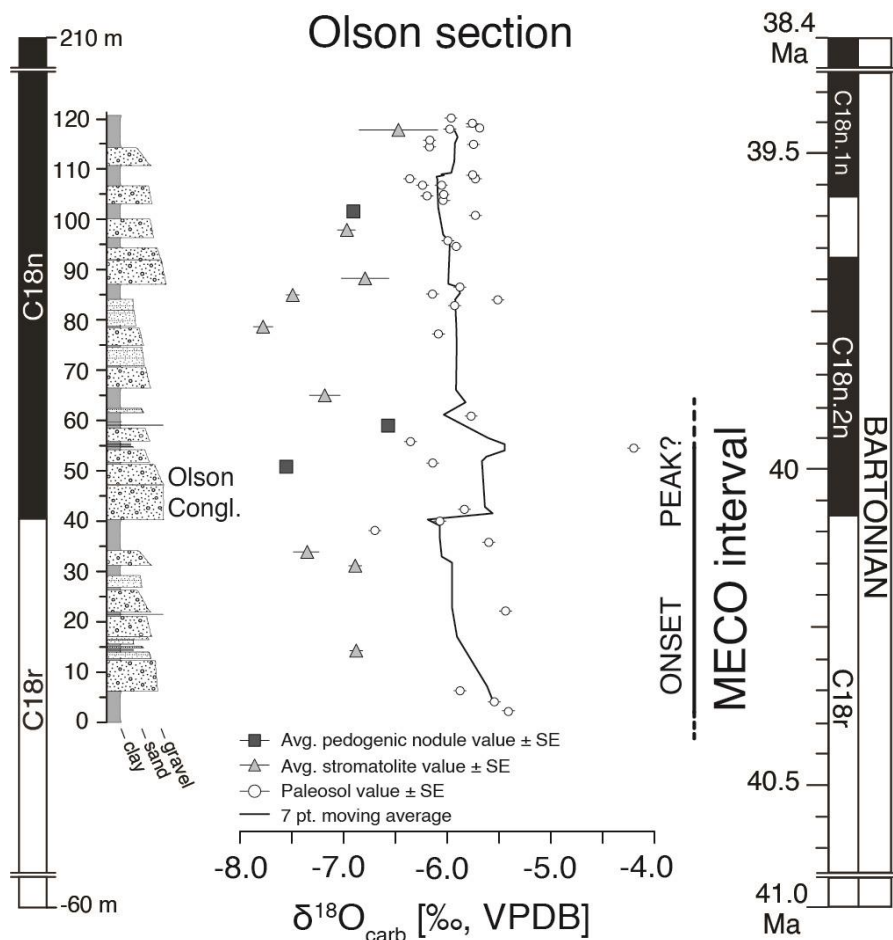
Figure 5. Oxygen isotope compositions ($\delta^{18}O_{carb}$) from paleosol bulk carbonates (white circles) with a 7-point moving average and associated standard error, and carbonate samples (stromatolites (triangles) and pedogenic nodules (squares)) for the Olsón section. Also marked is the MECO onset and peak interval based on $\delta^{13}C_{org}$ values from this study.

In summary, irrespective of the presence of authigenic and detrital carbonates in paleosol samples, the negative CIE in paleosol organic matter suggests that the MECO can be regionally recognized in the Escanilla Fm. Stable isotope data from the Escanilla Fm at Olsón is also compatible with climate perturbations through excursions similar to the isotope excursions in the marine records, even though there are differences in the magnitude of excursions. These excursions have also been identified downstream in the time-equivalent marine sediments in the Jaca Basin, Spain (Peris Cabré et al., 2023) indicating the preservation of MECO climate perturbation signals in the source-to-sink Escanilla sediment routing system.

4.3 Primary versus diagenetic signals

Carbon and oxygen isotope composition of bulk paleosol carbonates may be affected by the diagenetic alteration of mineral phases. It is therefore important to evaluate the potential diagenetic overprint on primary geochemical signatures (e.g., Marshall, 1992).

The degree of alteration was assessed through the relationship between $\delta^{13}C_{org}$ and $\delta^{13}C_{carb}$, and between $\delta^{18}O_{carb}$ and $\delta^{13}C_{carb}$ values. Pearson correlation coefficient, $r < 0.6$, indicates a statistically non-significant relationship and indicates that a diagenetic overprint on the primary signal can be excluded (e.g., Fio et al., 2010). In both correlation plots (Figure 6), no statistically significant correlation was found ($\delta^{13}C_{carb}$ vs $\delta^{13}C_{org}$: r = 0.21 ($P = .16$, N = 45), $\delta^{13}C_{carb}$ vs $\delta^{18}O_{carb}$: r = 0.05 ($P = .74$, N = 45)) indicating almost none or very minor diagenetic modification of the primary signal. Also, no correlation trend was observed between TOC and $\delta^{13}C_{org}$ (supplementary material; Figure S1).

Maximum Temperature (T_{max}) from rock eval analysis was used as a second approach to assess diagenetic alteration. T_{max} obtained in samples with high TOC (> 0.5 Wt. %) was < 440 °C which is the beginning of the oil window and indicates immature organic content (ca 60 °C, Espitalié et al., 1985).

As a third approach, paleosol samples (S9, S12, S17, S30) were analyzed using scanning electron microscopy (SEM). SEM images show presence of authigenic calcite (supplementary material, Figures S2 – S4), presence of authigenic clay minerals palygosrkite and smectite (supplementary material, Figures S5) and detrital illite and chlorite (supplementary material, Figures S6). Collectively, the three approaches suggest that the primary signal is largely preserved in the Escanilla Fm at Olsón.
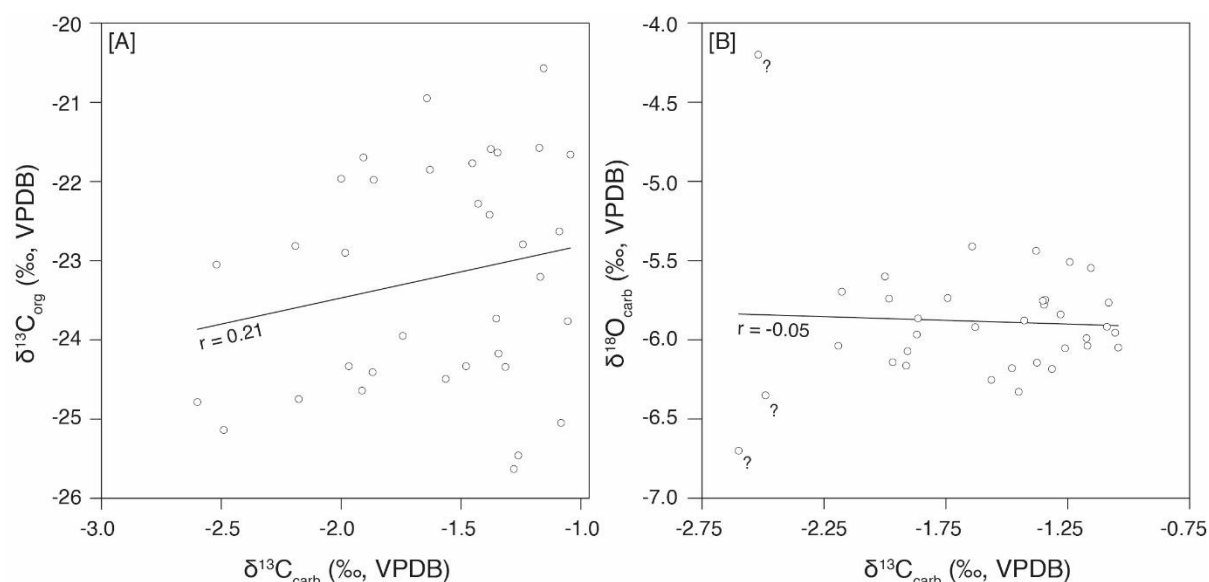
Figure 6. (**A**) Scatter plot of paleosol $\delta^{13}C_{carb}$ vs $\delta^{13}C_{org}$ values (**B**) Scatter plot of paleosol $\delta^{13}C_{carb}$ vs $\delta^{18}O_{carb}$ values. For both plots, Pearson correlation coefficient (r) and regression line is shown.

4.4 Weathering conditions

CIA values range from 9 ± 1 to 43 ± 1 % with an average value of 19 ± 1 % (N = 45). A slight peak in CIA values may represents peak weathering conditions during the MECO (Figure 7). CIA values have further been compared to CIW values (supplementary material; Figure S7), which takes into account potassium metasomatism, which range from 10 ± 1 to 48 ± 1 % with an average value of 20.5 ± 1 % (N = 45). Such low values are broadly indicative of weak chemical weathering, and if true, suggest a prevalence of physical weathering and erosion during the Middle Eocene. This contrasts with the assumption of intense weathering during global warming and recently published results for earlier hyperthermals (e.g., Tanaka et al., 2022). For instance, during the PETM, CIA values have been estimated to be in the $75 - 85$ % range (Stokke et al., 2021). Our relatively low CIA values at Olsón could be related to the long-term trend of low silicate weathering in response to elevated pCO$_2$ and warming levels during the Middle Eocene as indicated by osmium isotopes (van der Ploeg et al., 2018) and more recently by lithium isotope data available from the marine environment (Krause et al., 2023). Current understanding of the Earth's carbon cycle suggests strengthening of the negative silicate weathering feedback in response to rising atmospheric pCO$_2$ (Colbourn et al., 2015; Penman et al., 2020). However, the strength of the feedback depends primarily on several local/regional environmental variables such as temperature and precipitation, in addition to geomorphology and lithology (e.g., Richey et al., 2020; Deng et al., 2022). Our estimated weathering intensities are in line with a predicted dry and arid ecosystem (based on δ^{13}C$_{org}$ values) and therefore further reinforce our interpretation of a local dry and arid climate with a weakened hydrologic system in northern continental Spain during the Middle Eocene. Such low weathering rates, if confirmed at a scale relevant to the global carbon cycle, could also explain the sustained elevated carbon levels for a longer duration than during the previous hyperthermals, highlighting the different dynamics of the MECO (Sluijs et al., 2013; van der Ploeg et al., 2018).
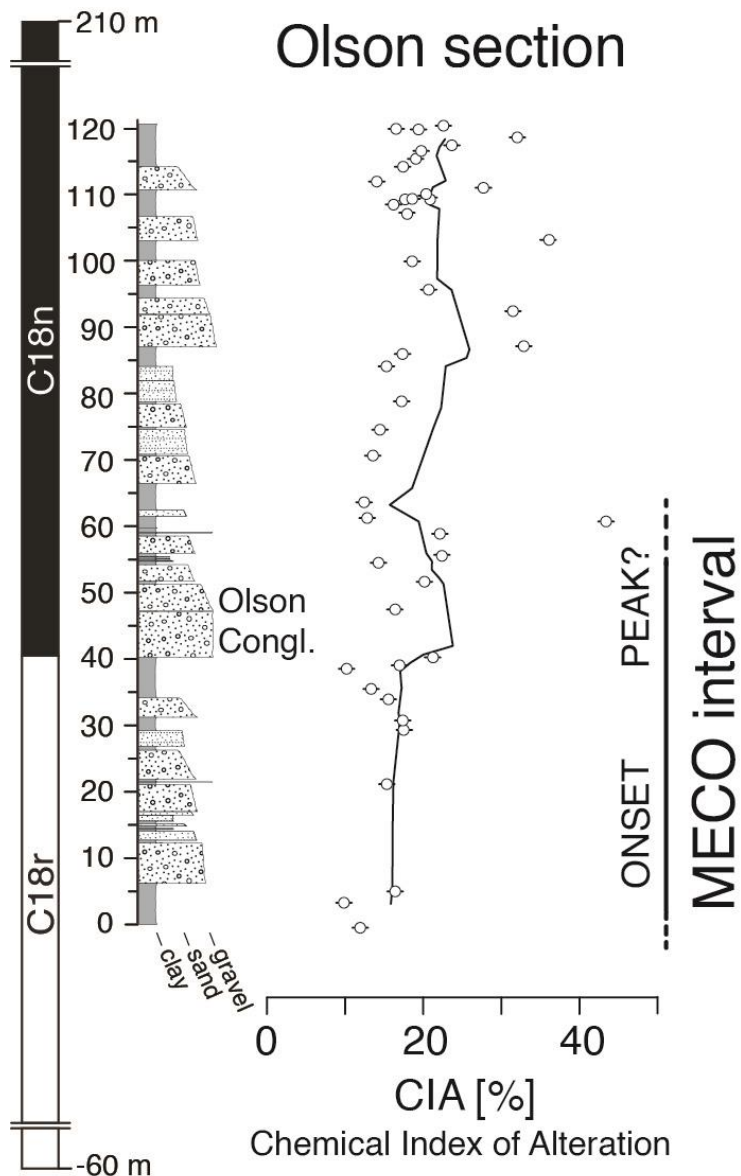
Figure 7. Chemical Index of Alteration (CIA) and associated standard error values from paleosols (white circles) displayed with a 7-point moving average to quantify chemical weathering in the Escanilla Fm at Olsón.

4.5 Regional climate record during the Middle Eocene

4.5.1 Mean annual precipitation (MAP) estimates

MAP values in the Olsón section range from 270 ± 10 to 570 ± 10 mm year^{-1} with an average of 330 ± 10 mm year^{-1}. Values stay constant at 300 ± 10 mm year^{-1} until 40 m followed by a 20 % increase in precipitation, up to 370 ± 10 mm year^{-1}, which most likely corresponds to the OC (peak MECO conditions). Above the OC, MAP values return to an average value of 340 ± 10 mm year^{-1} until the top of the section (Figure 8). Overall, these values predict arid to semi-arid climate in this area of the southern Pyrenees during the Middle Eocene and are coherent with the high $\delta^{13}C_{org}$ values (water-stressed environments), low CIA and CIW values (diminished

365   chemical weathering) in our section. At Igualada in the Ebro Basin, 200 km away from Olsón, palynological, pollen taxa and floral diversity studies suggest warm climate and humid vegetation, with preservation of mangrove swamp vegetation along the coast (Cavagnetto and Anadón 1996; Haseldonckx, 1972). The absence of humid climate in Olsón could be due to its location being higher in elevation and away from the coastline as compared to Igualada. Such regional differences in climate could also be the result of a climate transition phase during the

370   Middle Eocene, oscillating from a warm tropical Early Eocene to a cold and arid Early Oligocene, expressed differently in different regions and at possibly different sampled intervals.

    MAP estimates based on well-dated megafloras from the Weisselster and Lausitz Basins (both in northeast Germany), consisting of shallow marine and continental deposits, are in the range of 1100 to 1400 mm year^{-1} (Mosbrugger et al., 2005). Other proxy data from southern France indicate a MAP less than 500 mm year^{-1} in the

375   Bartonian (Kocsis et al., 2014), and is similar to our calculation from Spain. In conclusion, the values reported here should be regarded as being representative of a local signal, most likely influenced by rainshadow effects imposed by the Pyrenean topography at that time, which rose to 2000 meters between 49 and 41 Ma (Huyghe et al., 2012), thus possibly inducing orographic effects as observed in the modern situation (Vacherat et al., 2017; Huyghe et al., 2018).
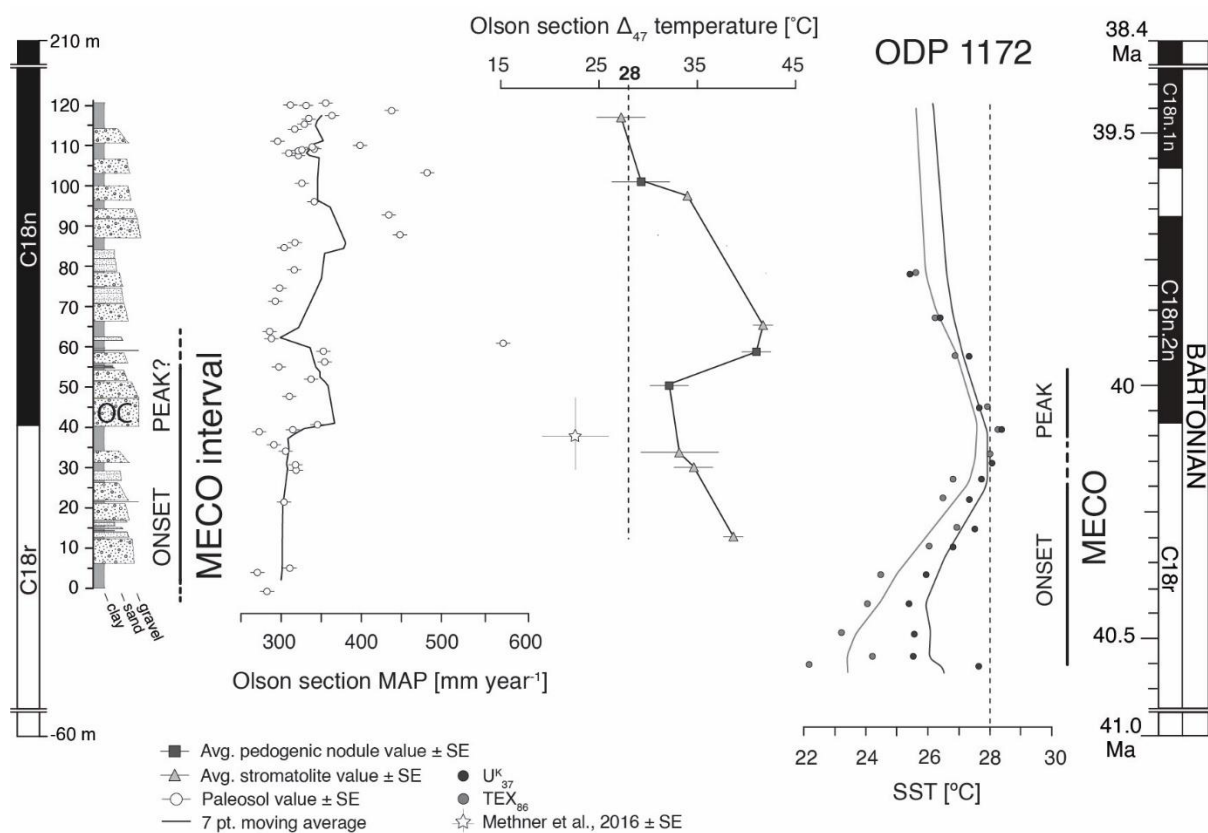
380

Figure 8. Mean annual precipitation (MAP) values (white circles) and the associated standard error from the Olsón section are presented using a 7-point moving average, followed by mean clumped isotope (Δ_{47}) temperatures and the standard error from replicate measurements of stromatolites (grey triangles) and pedogenic nodules (black squares). We compare our terrestrial temperature estimates to sea surface temperature proxies TEX_{86} and U^K_{37} (Bijl et al., 2010).

4.5.2 Carbonate clumped isotope thermometry

Δ_{47} values of carbonate in stromatolites have a range from 0.634 to 0.704 ‰, translating into temperatures of 18 to 43 °C (Figure 8). Each stromatolite was analyzed 2 to 4 times for replicate measurements with standard error ranging from 0.006 to 0.011 ‰. Δ_{47} values of carbonate in pedogenic nodules have a range from 0.629 to 0.704 ‰, translating into temperatures of 18 to 45 °C (Figure 8). Each pedogenic nodule was analyzed 4 to 8 times for replicate measurements having standard error ranging from 0.006 to 0.009 ‰.

While measurement reproducibility was good, care must be taken while interpreting Δ_{47} data as a number of potentially significant uncertainties are associated with it. For instance, Δ_{47} temperatures may not necessarily reflect primary formation temperatures but could instead be the result of a combination of primary formation temperatures and secondary effects such as potential diagenetic temperatures that bias primary compositions, although secondary overprinting is unlikely to produce cooler temperatures (Hren & Sheldon 2020). Secondly, organic contaminants could cause Δ_{47} values to be variable although any volatile part would be discarded when the samples were dried at high temperatures overnight (70 to 80 °C). Third, more replicate measurements from the same homogenized powder are required to assess interference by contaminants in the drilled powders and to better constrain the spread in data. For preliminary data such as the one presented here, the mean value could be considered as a good temperature estimate. Finally, significant diagenetic alteration could cause Δ_{47} values to be variable although a similar temperature range in both stromatolites and pedogenic nodules further suggests that analyzed samples most likely did not undergo significant diagenetic alteration after their formation. This would however need to be verified using petrography and/or cathodoluminescence.

Mean temperatures vary from 32.1 ± 1.8 °C to 38.6 ± 0.7 °C in the lower half of the section until 50 m followed by a peak mean temperature of 42 °C, just 25 m above the OC, without any observed change in lithology. Above 90 m until the top of the section, values return to an average value of 30 °C. Based on the available age constraints, our results suggest a potential lag between marine and terrestrial MECO climate signals. Our results also suggest a land-sea temperature gradient of 5 to 10 °C when compared to sea surface temperature (SST) records from ODP site 1172 (Tasmania, Pacific; Bijl et al., 2010), and IODP sites U1408 and U1410 (northwest Atlantic Ocean; van der Ploeg et al., 2023) most likely indicating an amplifying effect due to continentality. Similar continental temperature sensitivity during the Middle Eocene has also been previously identified through clumped

temperatures of pedogenic carbonates in the continental interiors of SW Montana, USA (Methner et al., 2016), Further research and sample analysis would however be required to investigate this further.

Δ_{47} temperatures were further used to calculate the $\delta^{18}O$ of fluids in equilibrium with carbonates using the temperature dependent fractionation factor of Epstein et al., (1953). Δ_{47} temperatures and $\delta^{18}O_{carb}$ values in stromatolites give water $\delta^{18}O$ values in the range of -5.9 to -2.1 ‰ (average of -3.3 ‰), while values from pedogenic nodules give water $\delta^{18}O$ values ranging from -6.5 to -0.8 ‰ (average of -3.6 ‰) (data in supplementary material). For comparison, we also used the approach by Kim & O'Neil (1997), which gave water $\delta^{18}O$ values from stromatolites to be in the range of -6.2 to -2.3 ‰ (average of -3.5 ‰) and -6.7 to -0.9 ‰ (average of -3.8 ‰) from pedogenic nodules (see supplementary material). These calculate water isotope values are consistent with meteoric water isotope composition at low latitude, but signify ^{18}O-isotope enrichment was most likely due to excess evapotranspiration under arid climatic conditions, consistent with estimates from other proxies used in this study.

4.5.3 Clay mineralogy

Clay mineral assemblages in paleosols are also important paleoclimatic indicators and reflect detrital mineral input, composition of the source area lithology, type of weathering of the source rocks, to provide integrated records of the overall climate (Singer 1984; Franke & Ehrmann 2010; Rego et al., 2018).

Smectite, palygorskite, illite, and chlorite form up to 98 % of the identified mineral assemblages in the studied section (Figure 9). Smectite, commonly derived from alteration of volcanic rocks, forms under seasonal rainfall conditions with a pronounced dry season (e.g., Singer, 1984; Tabor et al., 2014) and constitutes on average 17 % of the total identified clay mineral assemblage while individual values reach up to 58 %. Palygorskite, an authigenic mineral (supplementary material, Figure S5), is indicative of an arid to semi-arid environment where evapotranspiration exceeds precipitation (e.g., Birkeland, 1984; Singer, 2002; Meunier, 2005), and constitutes up to 25 % (average of 10 %) of the total clay mineral assemblage. Illite content is between 11 and 53 % (average of 36 %), while chlorite content is between 7 to 64 % (average of 35 %) in the analyzed paleosols. High amounts of illite and chlorite, both detrital minerals (supplementary material, Figure S6), are typically found in sediments formed by physical erosion of low-grade metamorphic rocks and are thus indicative of weak, incipient chemical weathering (Tabor et al., 2014; Rego et al., 2018), and support our calculated CIA values. Except for palygorskite, clay mineral variations can be inferred to reflect weathering conditions in the source area of the Escanilla sediment routing system.

Increase in authigenic palygorskite content above the OC indicates environmental conditions on land became drier which is in agreement with previous studies showing an increase in aridification following the MECO interval in NW China (Bosboom et al., 2014) and in the Neo-Tethys (Baskil section, eastern Turkey; Rego et al., 2018). This is also in agreement with our decreasing smectite/illite ratios above the OC (Figure 9) and is consistent with values reported by Rego et al. (2018). Overall, interpretation of clay mineral assemblages corroborates well with environmental conditions deduced from organic carbon stable isotopes data, weathering indices and mean annual precipitation.
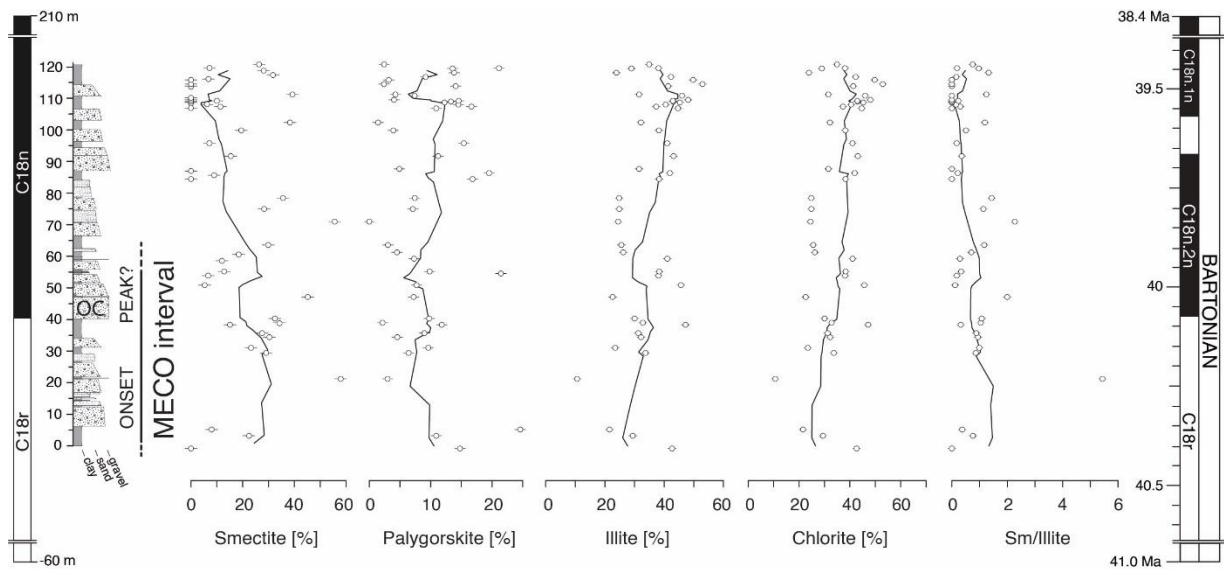
Figure 9. Identified clay mineral assemblages (smectite, palygorskite, illite, chlorite) and smectite/illite ratios are presented with respective standard error values and a 7-point moving average (black line) across the studied Escanilla Formation at Olsón. These minerals constitute up to 98% of the total clay mineralogy and suggest the presence of an arid to semi-arid climate under weak chemical weathering conditions during the MECO in the southern Pyrenees, Spain.

6 Conclusions

Detailed geochemical and mineralogical analysis of paleosols, stromatolites, and pedogenic nodules, provides new insights into terrestrial records of the MECO in the Ainsa Basin of the southern Pyrenees, Spain. A negative CIE measured on organic matter indicates the local preservation and identification of the MECO in the fluvial Escanilla Fm demonstrating that continental sedimentary successions can serve as important climate archives and highlighting stable isotope proxies as a powerful dating and correlation tool in notably difficult-to-date fluvial successions. Low CIA values in the Escanilla Formation suggest poor silicate weathering feedback in response to elevated pCO_2 levels and a prevalence of physical erosion during the Middle Eocene. This is compatible with an arid to semi-arid climate with a locally diminished hydrological cycle, as supported by low MAP estimates and

identified clay mineral assemblages in the fluvial sedimentary succession. Carbonate clumped isotope

465 thermometry suggests high temperatures up to 42 °C and a possible amplifying effect of 10 to 15 °C on continents

compared to temperature records from the deep sea.

References

1. Adatte, T., Stinnesbeck, W., and Keller, G.: Lithostratigraphic and mineralogic correlations of near K/T boundary clastic sediments in northeastern Mexico: implications for origin and nature of deposition.

470 Spec. Pap. Geol. Soc. Am., 307:211–226, 1996.

2. Anderson, N.T., Kelson, J.R., Kele, S., Daëron, M., Bonifacie, M., Horita, J., Mackey, T.J., John, C.M., Kluge, T., Petschnig, P., Jost, A.B., Huntington, K.W., Bernasconi, S.M., Bergmann, K.D.: A Unified clumped isotope thermometer calibration (0.5–1,100°C) using carbonate-based standardization. Geophys Res Lett 48. https://doi.org/10.1029/2020gl092069, 2021.

475 3. Awramik, S. M. and Buchheim, H. P.: Giant stromatolites of the Eocene Green River Formation (Colorado, USA), Geology, 43, 691–694, https://doi.org/10.1130/g36793.1, 2015

4. Barefoot, E.A., Nittrouer, J.A., Foreman, B.Z., Hajek, E.A., Dickens, G.R., Baisden, T., Toms, L.: Evidence for enhanced fluvial channel mobility and fine sediment export due to precipitation seasonality during the Paleocene-Eocene thermal maximum. Geology. https://doi.org/10.1130/g49149.1, 2021.

480 5. Behar, F., Beaumont, V., and Penteado, H. L. D. B.: Rock-Eval 6 Technology: Performances and Developments, Oil Gas Sci Technology, 56, 111–134, https://doi.org/10.2516/ogst:2001013, 2001.

6. Bentham, P. A., Talling, P. J., and Burbank, D. W.: Braided stream and flood-plain deposition in a rapidly aggrading basin: the Escanilla formation, Spanish Pyrenees, Geological Soc Lond Special Publ, 75, 177–194, https://doi.org/10.1144/gsl.sp.1993.075.01.11, 1993.

485 7. Bernasconi, S.M., Daëron, M., Bergmann, K.D., Bonifacie, M., Meckler, A.N., Affek, H.P., Anderson, N., Bajnai, D., Barkan, E., Beverly, E., Blamart, D., Burgener, L., Calmels, D., Chaduteau, C., Clog, M., Davidheiser-Kroll, B., Davies, A., Dux, F., Eiler, J., Elliott, B., Fetrow, A.C., Fiebig, J., Goldberg, S., Hermoso, M., Huntington, K.W., Hyland, E., Ingalls, M., Jaggi, M., John, C.M., Jost, A.B., Katz, S., Kelson, J., Kluge, T., Kocken, I.J., Laskar, A., Leutert, T.J., Liang, D., Lucarelli, J., Mackey, T.J.,

490 Mangenot, X., Meinicke, N., Modestou, S.E., Müller, I.A., Murray, S., Neary, A., Packard, N., Passey, B.H., Pelletier, E., Petersen, S., Piasecki, A., Schauer, A., Snell, K.E., Swart, P.K., Tripati, A., Upadhyay, D., Vennemann, T., Winkelstern, I, Yarian, D., Yoshida, N., Zhang, N., Ziegler, M.: InterCarb: A Community Effort to improve interlaboratory standardization of the carbonate clumped isotope

thermometer using carbonate standards. Geochem Geophys Geosystems 22, e2020GC009588. https://doi.org/10.1029/2020gc009588, 2021.

8. Bijl, P.K., Houben, A.J.P., Schouten, S., Bohaty, S.M., Sluijs, A., Reichart, G.-J., Damsté, J.S.S., Brinkhuis, H.: Transient Middle Eocene atmospheric CO2 and temperature variations. Science 330, 819–821. https://doi.org/10.1126/science.1193654, 2010.

9. Birkeland, P.W.: *Soils and geomorphology*. Oxford university press, 1984.

10. Bohaty, S.M., Zachos, J.C., Florindo, F., Delaney, M.L.: Coupled greenhouse warming and deep-sea acidification in the middle Eocene. Paleoceanography 24, PA2207. https://doi.org/10.1029/2008pa001676, 2009.

11. Bosboom, R.E., Abels, H.A., Hoorn, C., Berg, B.C.J. van den, Guo, Z., Dupont-Nivet, G.: Aridification in continental Asia after the Middle Eocene Climatic Optimum (MECO). Earth Planet Sc Lett 389, 34–42. https://doi.org/10.1016/j.epsl.2013.12.014, 2014

12. Cavagnetto, C., Anadón, P.: Preliminary palynological data on floristic and climatic changes during the Middle Eocene-Early Oligocene of the eastern Ebro Basin, northeast Spain. Rev Palaeobot Palyno 92, 281–305. https://doi.org/10.1016/0034-6667(95)00096-8, 1996.

13. Cerling, T.E., Quade, J.: Stable carbon and oxygen isotopes in soil carbonates, in: P.K. Swart, K.C. Lohmann, J. McKenzie, S. Savin (Eds.), Climate Change in Continental Isotopic Records, Geophysical Monograph, vol. 78, AGU, pp. 217 – 231, 1993.

14. Colbourn, G., Ridgwell, A., Lenton, T.M.: The time scale of the silicate weathering negative feedback on atmospheric CO2. Global Biogeochem Cy 29, 583–596. https://doi.org/10.1002/2014gb005054, 2015.

15. Deng, K., Yang, S., Guo, Y.: A global temperature control of silicate weathering intensity. Nat Commun 13, 1781. https://doi.org/10.1038/s41467-022-29415-0, 2022.

16. Dreyer, T., Fält, L.-M., Høy, T., Knarud, R., Steel, R. and Cuevas, J.-L.: Sedimentary Architecture of Field Analogues for Reservoir Information (SAFARI): A Case Study of the Fluvial Escanilla Formation, Spanish Pyrenees. In The Geological modelling of hydrocarbon reservoirs and outcrop analogues (eds S.S. Flint and I.D. Bryant). https://doi.org/10.1002/9781444303957.ch3, 1992.

17. Epstein, S., Buchsbaum, R., Lowenstam, H.A. and Urey, H.C.: Revised carbonate-water isotopic temperature scale. GSA Bulletin 64, 1315-1326. https://doi.org/10.1130/0016-7606(1953)64(1315:RCITS)2.0.CO;2, 1953

18. Espitalié, J., Deroo, G., and Marquis, F.: Rock-Eval pyrolysis and its applications, Revue De L'Institut Français Du Petrole, 40, 563–579, 10.2516/ogst:1985045, 1985.

19. Fio, K., Spangenberg, J. E., Vlahović, I., Sremac, J., Velić, I., and Mrinjek, E.: Stable isotope and trace element stratigraphy across the Permian–Triassic transition: A redefinition of the boundary in the Velebit Mountain, Croatia, Chem. Geol., 278, 38–57, https://doi.org/10.1016/j.chemgeo.2010.09.001, 2010,

20. Foreman, B.Z., Heller, P.L., Clementz, M.T.: Fluvial response to abrupt global warming at the Palaeocene/Eocene boundary. Nature 491, 92–95. https://doi.org/10.1038/nature11513, 2012.

21. Franke, D. and Ehrmann, W.: Neogene clay mineral assemblages in the AND-2A drill core (McMurdo Sound, Antarctica) and their implications for environmental change, Palaeogeogr., Palaeoclim., Palaeoecol., 286, 55–65, https://doi.org/10.1016/j.palaeo.2009.12.003, 2010.

22. Gandolfi, A., Giraldo-Gomez, V. M., Luciani, V., Piazza, M., Adatte, T., Arena, L., Bomou, B., Fornaciari, E., Frijia, G., Kocsis, L., and Briguglio, A.: The Middle Eocene Climatic Optimum (MECO) impact on the benthic and planktic foraminiferal resilience from a shallow-water sedimentary record, Riv. Ital. DI Paléontol. E Strat., 129, https://doi.org/10.54103/2039-4942/20154, 2023.

23. Garcés, M., López-Blanco, M., Silva, R., Juvany, P., Arbués, P., Pueyo, E., and Beamud, E.: The record of the Middle Eocene Climate Optimum in the carbonate platforms of the South Pyrenean Basin (Santo Domingo, External Sierras), https://doi.org/10.5194/egusphere-egu23-8739, 2023.

24. Gran, K., Paola, C.: Riparian vegetation controls on braided stream dynamics. Water Resour Res 37, 3275–3283. https://doi.org/10.1029/2000wr000203, 2001.

25. Harnois, L.: The CIW index: A new chemical index of weathering, Sediment Geol, 55, 319–322, https://doi.org/10.1016/0037-0738(88)90137-6, 1988.

26. Haseldonckx, P.: The presence of Nypa palms in Europe: a solved problem. Geol, 1972.

27. Henehan, M.J., Edgar, K.M., Foster, G.L., Penman, D.E., Hull, P.M., Greenop, R., Anagnostou, E., Pearson, P.N.: Revisiting the Middle Eocene Climatic Optimum "carbon cycle conundrum" with new estimates of atmospheric pCO2 from boron isotopes. Paleoceanogr Paleoclimatology 35. https://doi.org/10.1029/2019pa003713, 2020.

28. Hren, M.T., Sheldon, N.D.: Terrestrial microbialites provide constraints on the mesoproterozoic atmosphere. Depositional Rec 6, 4–20. https://doi.org/10.1002/dep2.79, 2020.

29. Huyghe, D., Mouthereau, F., and Emmanuel, L.: Oxygen isotopes of marine mollusc shells record Eocene elevation change in the Pyrenees, Earth Planet Sc Lett, 345–348, 131–141, https://doi.org/10.1016/j.epsl.2012.06.035, 2012.

555   30. Huyghe, D., Mouthereau, F., Sébilo, M., Vacherat, A., Ségalen, L., Richard, P., Biron, P., Bariac, T.: Impact of topography, climate and moisture sources on isotopic composition (δ 18O & δD) of rivers in the Pyrenees: Implications for topographic reconstructions in small orogens. Earth Planet Sc Lett 484, 370–384. https://doi.org/10.1016/j.epsl.2017.12.035, 2018.

31. Jovane, L., Florindo, F., Coccioni, R., Dinarès-Turell, J., Marsili, A., Monechi, S., Roberts, A.P.,
560   Sprovieri, M.: The middle Eocene climatic optimum event in the Contessa Highway section, Umbrian Apennines, Italy. Gsa Bulletin 119, 413–427. https://doi.org/10.1130/b25917.1, 2007.

32. Kim, S. T. and O'Neil, J. R.: Equilibrium and nonequilibrium oxygen isotope effects in synthetic carbonates, Geochim Cosmochim Ac, 61, 3461–3475, https://doi.org/10.1016/s0016-7037(97)00169-5, 1997.

565   33. Kocsis, L., Ozsvárt, P., Becker, D., Ziegler, R., Scherler, L., Codrea, V.: Orogeny forced terrestrial climate variation during the late Eocene–early Oligocene in Europe. Geology 42, 727–730. https://doi.org/10.1130/g35673.1, 2014.

34. Kohn, M.J.: Carbon isotope compositions of terrestrial C3 plants as indicators of (paleo)ecology and (paleo)climate. Proc National Acad Sci 107, 19691–19695. https://doi.org/10.1073/pnas.1004933107,
570   2010.

35. Krause, A. J., Sluijs, A., Ploeg, R. van der, Lenton, T. M., and Strandmann, P. A. E. P. von: Enhanced clay formation key in sustaining the Middle Eocene Climatic Optimum, Nat. Geosci., 16, 730–738, https://doi.org/10.1038/s41561-023-01234-y, 2023.

36. Labourdette, R., Jones, R.R.: Characterization of fluvial architectural elements using a three-dimensional
575   outcrop data set: Escanilla braided system, South-Central Pyrenees, Spain. Geosphere 3, 422–434. https://doi.org/10.1130/ges00087.1, 2007.

37. Labourdette, R.: Stratigraphy and static connectivity of braided fluvial deposits of the lower Escanilla Formation, south central Pyrenees, Spain, Aapg Bull, 95, 585–617, https://doi.org/10.1306/08181009203, 2011.

580   38. Lupker, M., France-Lanord, C., Lavé, J., Bouchez, J., Galy, V., Métivier, F., Gaillardet, J., Lartiges, B., and Mugnier, J.: A Rouse-based method to integrate the chemical composition of river sediments:

Application to the Ganga basin, J. Geophys. Res.: Earth Surf., 116, https://doi.org/10.1029/2010jf001947, 2011.

39. Marshall, J. D.: Climatic and oceanographic isotopic signals from the carbonate rock record and their preservation, Geol. Mag., 129, 143–160, https://doi.org/10.1017/s0016756800008244, 1992.

40. Methner, K., Mulch, A., Fiebig, J., Wacker, U., Gerdes, A., Graham, S.A., Chamberlain, C.P.: Rapid Middle Eocene temperature change in western North America. Earth Planet Sc Lett 450, 132–139. https://doi.org/10.1016/j.epsl.2016.05.053, 2016.

41. Meunier, A.: Clays in sedimentary environments. *Clays*, pp.295-327. Mijnb. 51, 645–650, 2005.

42. Michael, N. A., Whittaker, A. C., and Allen, P. A.: The Functioning of Sediment Routing Systems Using a Mass Balance Approach: Example from the Eocene of the Southern Pyrenees, J Geology, 121, 581–606, https://doi.org/10.1086/673176, 2013.

43. Michael, N. A., Whittaker, A. C., Carter, A., and Allen, P. A.: Volumetric budget and grain-size fractionation of a geological sediment routing system: Eocene Escanilla Formation, south-central Pyrenees, Gsa Bulletin, 126, 585–599, https://doi.org/10.1130/b30954.1, 2014.

44. Mosbrugger, V., Utescher, T., Dilcher, D.L.: Cenozoic continental climatic evolution of Central Europe. P Natl Acad Sci Usa 102, 14964–14969. https://doi.org/10.1073/pnas.0505267102, 2005.

45. Mulch, A., Chamberlain, C.P., Cosca, M.A., Teyssier, C., Methner, K., Hren, M.T., Graham, S.A.: Rapid change in high-elevation precipitation patterns of western North America during the Middle Eocene Climatic Optimum (MECO). Am J Sci 315, 317–336. https://doi.org/10.2475/04.2015.02, 2015.

46. Nesbitt, H.W., Young, G.M.: Early Proterozoic climates and plate motions inferred from major element chemistry of lutites. Nature 299, 715–717. https://doi.org/10.1038/299715a0, 1982.

47. Ogg, J.G.: Geologic Time Scale 2020 159–192. https://doi.org/10.1016/b978-0-12-824360-2.00005-x, 2020.

48. Parsons, A. J., Michael, N. A., Whittaker, A. C., Duller, R. A., and Allen, P. A.: Grain-size trends reveal the late orogenic tectonic and erosional history of the south–central Pyrenees, Spain, J Geol Soc London, 169, 111–114, https://doi.org/10.1144/0016-76492011-087, 2012.

49. Penman, D.E., Rugenstein, J.K.C., Ibarra, D.E., Winnick, M.J.: Silicate weathering as a feedback and forcing in Earth's climate and carbon cycle. Earth-sci Rev 209, 103298. https://doi.org/10.1016/j.earscirev.2020.103298, 2020.

50. Peris Cabré, S., Valero, L., Spangenberg, J. E., Vinyoles, A., Verité, J., Adatte, T., Tremblin, M., Watkins, S., Sharma, N., Garcés, M., Puigdefàbregas, C., and Castelltort, S.: Fluvio-deltaic record of increased sediment transport during the Middle Eocene Climatic Optimum (MECO), Southern Pyrenees, Spain, Clim. Past, 19, 533–554, https://doi.org/10.5194/cp-19-533-2023, 2023.

51. Ploeg, R. van der, Cramwinckel, M.J., Kocken, I.J., Leutert, T.J., Bohaty, S.M., Fokkema, C.D., Hull, P.M., Meckler, A.N., Middelburg, J.J., Müller, I.A., Penman, D.E., Peterse, F., Reichart, G.-J., Sexton, P.F., Vahlenkamp, M., Vleeschouwer, D.D., Wilson, P.A., Ziegler, M., Sluijs, A.: North Atlantic surface ocean warming and salinization in response to middle Eocene greenhouse warming. Sci Adv 9, eabq0110. https://doi.org/10.1126/sciadv.abq0110, 2023.

52. Ploeg, R. van der, Selby, D., Cramwinckel, M.J., Li, Y., Bohaty, S.M., Middelburg, J.J., Sluijs, A.: Middle Eocene greenhouse warming facilitated by diminished weathering feedback. Nat Commun 9, 2877. https://doi.org/10.1038/s41467-018-05104-9, 2018.

53. Rego, E. S., Jovane, L., Hein, J. R., Sant'Anna, L. G., Giorgioni, M., Rodelli, D., and Özcan, E.: Mineralogical evidence for warm and dry climatic conditions in the Neo-Tethys (eastern Turkey) during the middle Eocene, Palaeogeogr Palaeoclim Palaeoecol, 501, 45–57, https://doi.org/10.1016/j.palaeo.2018.04.007, 2018.

54. Richey, J.D., Montañez, I.P., Goddéris, Y., Looy, C.V., Griffis, N.P., DiMichele, W.A.: Influence of temporally varying weatherability on CO2-climate coupling and ecosystem change in the late Paleozoic. Clim Past 16, 1759–1775. https://doi.org/10.5194/cp-16-1759-2020, 2020.

55. Schulze, E.-D., Ellis, R., Schulze, W., Trimborn, P., Ziegler, H.: Diversity, metabolic types and δ13C carbon isotope ratios in the grass flora of Namibia in relation to growth form, precipitation and habitat conditions. Oecologia 106, 352–369. https://doi.org/10.1007/bf00334563, 1996.

56. Sharma, N., Whittaker, A.C., Watkins, S.E., Valero, L., Vérité, J., Puigdefabregas, C., Adatte, T., Garcés, M., Guillocheau, F., Castelltort, S.: Water discharge variations control fluvial stratigraphic architecture in the Middle Eocene Escanilla Formation, Spain. Sci Rep 13, 6834. https://doi.org/10.1038/s41598-023-33600-6, 2023.

57. Sheldon, N.D., Retallack, G.J., Tanaka, S.: Geochemical climofunctions from north American soils and application to paleosols across the Eocene-Oligocene Boundary in Oregon. J Geology 110, 687–696. https://doi.org/10.1086/342865, 2002.

640   58. Singer, A.: Palygorskite and Sepiolite. In Soil Mineralogy with Environmental Applications (eds J.B. Dixon and D.G. Schulze). https://doi.org/10.2136/sssabookser7.c18, 2002.

59. Singer, A.: The paleoclimatic interpretation of clay minerals in sediments — a review. Earth-sci Rev 21, 251–293. https://doi.org/10.1016/0012-8252(84)90055-2, 1984.

60. Sluijs, A., Zeebe, R.E., Bijl, P.K., Bohaty, S.M.: A middle Eocene carbon cycle conundrum. Nat Geosci 645   6, 429–434. https://doi.org/10.1038/ngeo1807, 2013.

61. Spangenberg, J.E.: Bulk C, H, O, and fatty acid C stable isotope analyses for purity assessment of vegetable oils from the southern and northern hemispheres. Rapid Commun Mass Sp 30, 2447–2461. https://doi.org/10.1002/rcm.7734, 2016.

62. Spangenberg, J.E.: Carbon and oxygen isotope working standards from C3 and C4 photosynthates. Isot 650   Environ Healt S 42, 231–238. https://doi.org/10.1080/10256010600841059, 2006.

63. Spofforth, D.J.A., Agnini, C., Pälike, H., Rio, D., Fornaciari, E., Giusberti, L., Luciani, V., Lanci, L., Muttoni, G.: Organic carbon burial following the middle Eocene climatic optimum in the central western Tethys. Paleoceanography 25. https://doi.org/10.1029/2009pa001738, 2010.

64. Spötl, C., Vennemann, T.W.: Continuous-flow isotope ratio mass spectrometric analysis of carbonate 655   minerals. Rapid Commun. Mass Spectrom. 17, 1004–1006. https://doi.org/10.1002/rcm.1010, , 2003.

65. Stein, R.A., Sheldon, N.D., Allen, S.E., Smith, M.E., Dzombak, R.M., Jicha, B.R. Climate and ecology in the Rocky Mountain interior after the early Eocene Climatic Optimum. Clim Past 17, 2515–2536. https://doi.org/10.5194/cp-17-2515-2021, 2021.

66. Stokke, E.W., Jones, M.T., Riber, L., Haflidason, H., Midtkandal, I., Schultz, B.P., Svensen, H.H.: Rapid 660   and sustained environmental responses to global warming: the Paleocene–Eocene Thermal Maximum in the eastern North Sea. Clim Past 17, 1989–2013. https://doi.org/10.5194/cp-17-1989-2021, 2021.

67. Tabor, N.J., Myers, T.S.: Paleosols as indicators of paleoenvironment and paleoclimate. Annu Rev Earth Pl Sc 43, 1–29. https://doi.org/10.1146/annurev-earth-060614-105355, 2014.

68. Tanaka, E., Yasukawa, K., Ohta, J., Kato, Y.: Enhanced continental chemical weathering during the 665   multiple early Eocene hyperthermals: New constraints from the southern Indian Ocean. Geochim Cosmochim Ac 331, 192–211. https://doi.org/10.1016/j.gca.2022.05.022, 2022.

69. Tyson, R.V.: Sedimentary Organic Matter, Organic Facies and Palynofacies. Hapman and Hall, London, 615. https://doi.org/10.1007/978-94-011-0739-6, 1995.

70. Vacherat, A., Mouthereau, F., Pik, R., Huyghe, D., Paquette, J.-L., Christophoul, F., Loget, N., Tibari, B. : Rift-to-collision sediment routing in the Pyrenees: A synthesis from sedimentological, geochronological and kinematic constraints. Earth-sci Rev 172, 43–74. https://doi.org/10.1016/j.earscirev.2017.07.004, 2017.

71. Vincent, S. J.: The Sis palaeovalley: a record of proximal fluvial sedimentation and drainage basin development in response to Pyrenean mountain building, Sedimentology, 48, 1235--1276, https://doi.org/10.1046/j.1365-3091.2001.00421.x, 2001.

72. Vinyoles, A., López-Blanco, M., Garcés, M., Arbués, P., Valero, L., Beamud, E., Oliva-Urcia, B., Cabello, P.: 10 Myr evolution of sedimentation rates in a deep marine to non-marine foreland basin system: Tectonic and sedimentary controls (Eocene, Tremp–Jaca Basin, Southern Pyrenees, NE Spain). Basin Res. https://doi.org/10.1111/bre.12481, 2020.

73. Whittaker, A. C., Duller, R. A., Springett, J., Smithells, R. A., Whitchurch, A. L., and Allen, P. A.: Decoding downstream trends in stratigraphic grain size as a function of tectonic subsidence and sediment supply, Geol Soc Am Bull, 123, 1363–1382, https://doi.org/10.1130/b30351.1, 2011.

74. Zamarreño, I., Anadón, P., Utrilla, R.: Sedimentology and isotopic composition of Upper Palaeocene to Eocene non-marine stromatolites, eastern Ebro Basin, NE Spain. Sedimentology 44, 159–176. https://doi.org/10.1111/j.1365-3091.1997.tb00430.x, 1997.

Acknowledgements

We acknowledge support from the Swiss National Science Foundation (SNSF) for grant 200020_182017: Earth Surface Signaling Systems 2 awarded to Sébastien Castelltort.

Author contributions

NS led fieldwork, sample preparation, data interpretation, and writing. JES performed stable-isotope analyses, data interpretation, discussion and writing. TA performed XRD analyses, data interpretation, and discussion. TV and LK performed clumped isotope analyses, and contributed to the discussion and editing. JV and LV contributed to fieldwork, review and editing. SC conceptualized and supervised the projet, acquired funding, contributed to the interpretation and writing.

Competing interests

The authors declare no competing interests.

Data availability

All data from this study are provided within the manuscript and accompanying supplementary material.